Supporting Information: Monitoring the impact of EU F-gas regulation on HFC-134a emissions through a comparison of top-down and bottom-up estimates

Saurabh Annadate[1,2,3*], Enrico Mancinelli[1], Barbara Gonella[4], Federica Moricci[4], Simon O'Doherty[5], Kieran Stanley[5], Dickon Young[5], Martin K. Vollmer[6], Rita Cesari[7], Serena Falasca[8], Umberto Giostra[1], Michela Maione[1,3], Jgor Arduini[1,3*]

[1]Department of Pure and Applied Sciences, University of Urbino "Carlo Bo", Urbino, 61029, Italy.
[2]University School for Advanced Studies IUSS Pavia, Italy.
[3]Institute of Atmospheric Sciences and Climate, National Research Council, Bologna, Italy.
[4]Institute for Environmental Protection and Research (ISPRA), Rome, Italy.
[5]School of Chemistry, University of Bristol, Bristol, BS8 1TS, UK.
[6]Laboratory for Air Pollution and Environmental Technology, Empa, Swiss Federal Laboratories for Materials Science and Technology, Dübendorf 8600, Switzerland.
[7]Institute of Atmospheric Sciences and Climate, National Research Council, Lecce, Italy.
[8]Department of Physics, Sapienza University of Rome, 00185 Rome, Italy.

*Corresponding author(s). E-mail(s): saurabh.annadate@iusspavia.it; jgor.arduini@uniurb.it;

Table 1: Measurement sites information.

Site name	Country	Latitude (°N)	Longitude (°E)	Altitude (m)	Years obs. available
Monte Cimone	Italy	44.18	10.70	2165	2008-2023
Jungfraujoch	Switzerland	46.55	7.98	3580	2008-2023
Tacolneston	United Kingdom	52.52	1.139	56	2012-2023
Mace Head	Republic of Ireland	53.33	-9.90	8	2008-2023

1 Global and regional regulations

In Europe, fluorinated greenhouse gases (F-gases) are controlled under Regulation on Fluorinated Greenhouse Gases (EU) No 573/2024 of the European Parliament and of the Council, issued on 7 February 2024, amending Directive (EU) 2019/1937 and repealing Regulation (EU) No 517/2014. This regulation aims to curtail high-GWP fluorinated substances use by establishing a phase-down program, gradually reducing the quantity of HFCs placed on the EU market. The EU Regulation on F-gases asks for a complete phase-out of the consumption of HFCs by 2050, and a phase-down to a minimum (15%) as of 2036 of the production rights allocated by the Commission. Moreover, the EU Regulation imposes stricter rules to prevent leakages from transportation to disposal of equipment and products. This also complies with the 2016 Kigali amendment of the 1987 Montreal Protocol on Substances that Deplete the Ozone Layer, which entered into force on 1 January 2019 and was ratified by more than 140 countries. Under the amendment, countries commit to cutting HFC production and consumption by more than 80% over the next 30 years to avoid more than 70 billion metric tonnes of CO2 equivalent emissions by 2050. The amendment will save up to 0.4 °C of additional warming by the end of the century.S3 Figure S1 presents the total EU HFC-134a supply over the years, highlighting progress under the EU HFC phase-down.

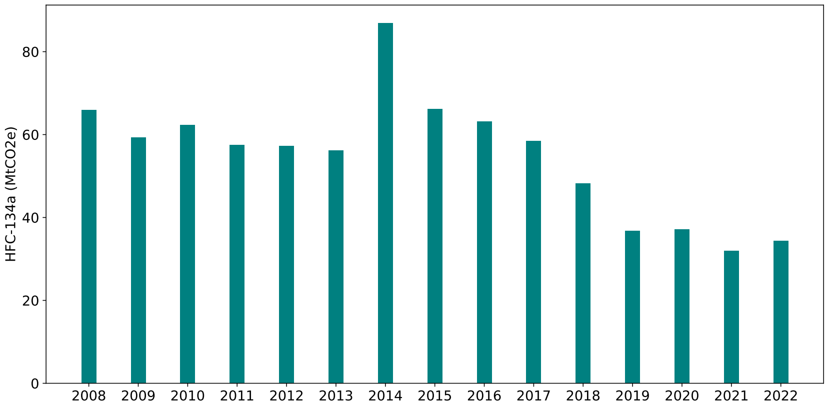

Fig. 1: The total EU HFC-134a supply for the period of 2008-2022. Own elaboration based on data from Fluorinated greenhouse gases reports by the European Environment Agency [2].

2 Measurement network

Fig. 2 shows the measurement sites of Monte Cimone (CMN), Jungfraujoch (JFJ), Tacolneston (TAC), and Mace Head (MHD). At JFJ, MHD, and TAC, 2 l of air sample is pre-concentrated at low temperatures ($-165°$C and $-180°$C) in a two-trap system (Medusa)[5]. At CMN the pre-concentration of 1 l of air is achieved by a Markes Unity2/ AirServer2 thermal desorption device[4] at the temperature of $-30°$C. In both systems, after pre-concentration, the analytes are desorbed into a GC (Agilent 6890N), using helium (He 6.0) as the carrier gas, and detected by quadrupole electron ionisation mass spectrometer (Agilent 5975C) in selected ion mode (SIM). Chromatographic separation is achieved with a CP-PoraBOND Q column (0.32mm i.d.x25m, 5μm film thickness, Agilent) at JFJ, MHD, and TAC while a GasPro plot column (0.32mm i.d.x30m, Agilent) is used at CMN station. A custom Linux-based software, GCWerks, provides both instrument control and data processing.

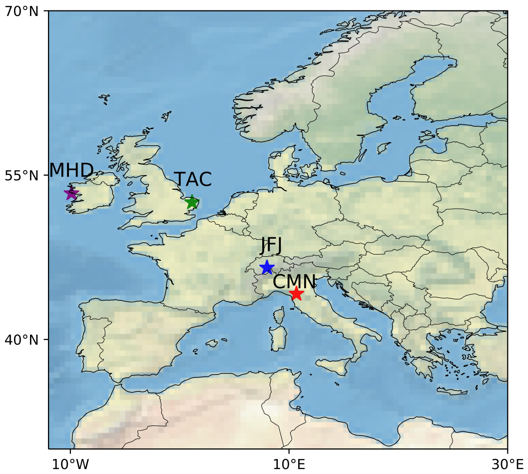

Fig. 2: Inversion domain and locations of Monte Cimone (CMN), Jungfraujoch (JFJ), Tacolneston (TAC), and Mace Head (MHD) surface in-situ measurement sites that are part of the AGAGE network.

3 Bayesian inversion

To derive the top-down emissions of HFC-134a from the European domain, high-frequency trace gas atmospheric measurements were combined with a high-resolution atmospheric transport model. The Lagrangian Particle Dispersion Models (LPDMs) are widely used in inverse modelling for computing source-receptor relationships (SRRs)[1]. In this study, we use FLEXPART v10.4 operated backward-in-time, in a receptor-oriented mode to simulate the transport of the particles starting from the measurement sites. The FLEXPART model is driven by the 3-hourly ERA5 meteorology data at a horizontal resolution of 0.28°. 10000 virtual particles are released from the receptor sites for each measurement and tracked for 10 days backwards in time. For a receptor, the SRR depends on the average residence time (RT) of back-trajectories within 100 meters from the surface, assuming emissions occur solely at the surface level. The SRRs also commonly known as "footprints", relate the surface emissions to the observed mixing ratio throughout the backward simulation time frame. By multiplying the footprint with an emission map and integrating over space and time we get simulated mixing ratios as initially shown by Seibert and Frank [6]. The SRR output is stored at the resolution of 0.5° × 0.5° which makes up the partial sensitivity operator($\mathbf{H}$). The relationship between observed mixing ratio $\mathbf{y}$, total sensitivity operator $\mathbf{H}$, and the state vector $\mathbf{x}$ is given by:

$$\mathbf{y} = \mathbf{Hx} + \epsilon \tag{1}$$

where $\mathbf{y} = (y_1 ... y_m)$ is a vector of observed mixing ratios, with m being the total number of observations; $\mathbf{x} = (x_1 ... x_n)$ is the state vector of gridded emissions and background mixing ratio scalars, where n is the total number of state vector elements; $\mathbf{H}$ is the total sensitivity operator with components of the atmospheric transport (e.g., SRRs) to each receptor and the background mixing ratios corresponding to each observation (with dimension $m \times n$), and ϵ is the sum of observation and model errors. The state vector $\mathbf{x}$ can be very large for a high-resolution flux matrix. Therefore, we use a variable resolution grid to reduce the dimensionality of the inversion. The variable resolution grid is based on the SRRs and the prior flux matrix (for a detailed description see Thompson and Stohl [9]). We have used the analytical solution method in FLEXINVERT+ which minimises $\mathbf{J(x)}$ to give the posterior estimate of the state vector as,

$$\mathbf{x} = \mathbf{x_b} + \mathbf{BH}^T(\mathbf{HBH}^T + \mathbf{R})^{-1}(\mathbf{y} - \mathbf{Hx}) \tag{2}$$

The HFC-134a is a non-reactive gas with no natural sinks over land. However, the inversion system can produce non-physical negative emission fluxes owing to the assumption of Gaussian distribution of fluxes. This has been handled by applying an inequality constraint on the *a posteriori* fluxes using the truncated Gaussian approach by Thacker [8]. In this step, an inequality constraint is implemented, specifically requiring that emissions remain at or above zero. Refer to Thompson and Stohl [9] for more details.

4 Sensitivity tests performed using synthetic emissions

We conducted a series of synthetic data experiments to evaluate the capabilities of the inversion system to analyse the seasonality and inter-annual variability in emission estimates. For these experiments, we prepared a synthetic emission field based on the EDGAR 2008 emission flux. We added a monthly varying seasonality to the EDGAR 2008 emission that gradually increased each month and peaked in June and July by 40% of the base emissions. This field, referred to as "synthetic-true" emissions (shown in blue in Fig. 3), was then used to generate "synthetic observations" by multiplying the FLEXPART sensitivity with the synthetic-true emission fields and adding background mole fractions calculated using REBS method. We then added normally distributed perturbations to prepare the final synthetic observations. In the synthetic data experiments, we prepared the synthetic observations using the same FLEXPART sensitivities and background mixing ratios that were used in the inversion. This ensures that these factors are perfectly known, thereby eliminating any errors arising from transport and background in the synthetic inversions.

To understand the effect of the prior emission fluxes on the inversion estimates, we performed monthly inversions using both aseasonal (Fig. 3a) and seasonally varying priors (Fig. 3b). While the inversion system proved robust regardless of whether an aseasonal or seasonal prior was used, incorporating seasonal prior enhanced the accuracy of the posterior emissions, particularly given that the synthetic true emissions also had seasonality.

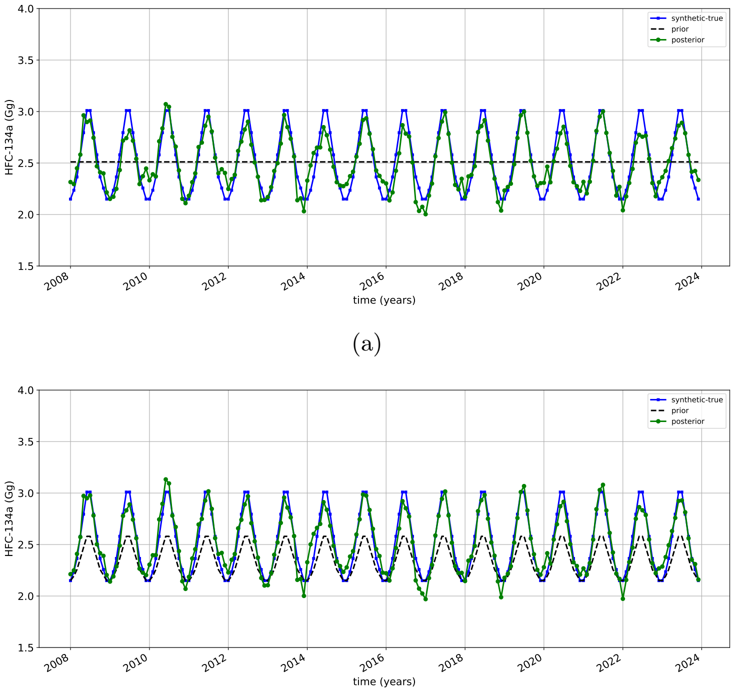

(a)

(b)

Fig. 3: The monthly Italian HFC-134a emissions are presented for synthetic-true (blue), prior (black), and posterior (green) fluxes. The top panel illustrates the emissions for the inversion performed using aseasonal prior emissions, while the bottom panel depicts the case with seasonal prior emissions.

The magnitude of noise added to the synthetic observations determines the extent of model-data mismatch errors in the inversion. We conducted yearly inversions using synthetic observations with both high and low magnitudes of noise, as shown in Fig. 4. The inversion system consistently performs well with observations that have lower model-data mismatch errors. High model-data mismatch errors result in significant yearly variations in the Italian posterior inversion estimates as shown in Fig 4a. The inversion system assumes a Gaussian distribution for model-data mismatch errors and is highly influenced by observations at the tail of the distribution [9]. Especially for mountain stations, where complex orography leads to poorly resolved transport processes. Up-slope flows can bring polluted air from valleys, resulting in biased low prior

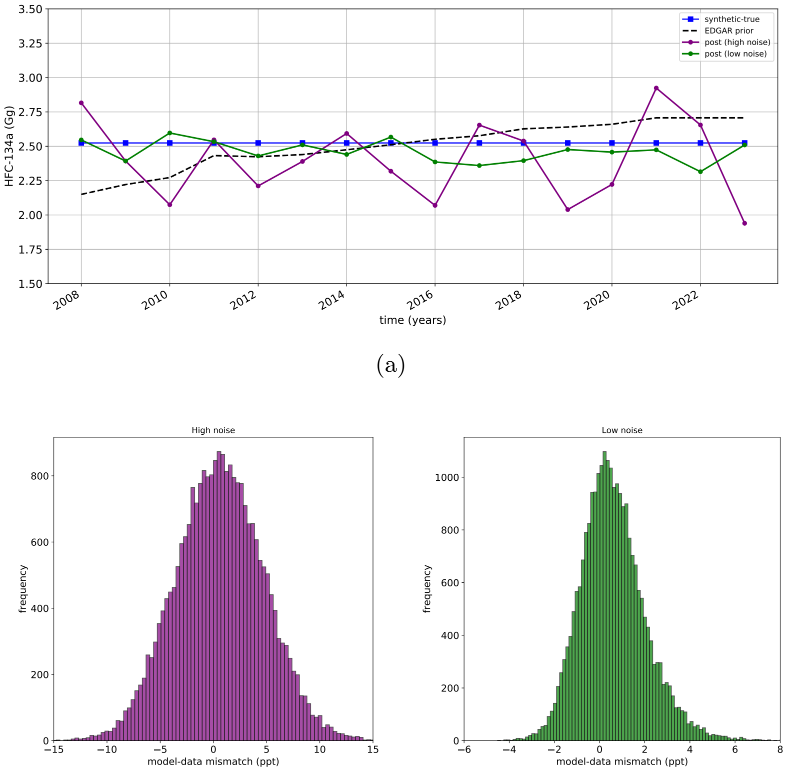

(a)

(b) (c)

Fig. 4: (a) Yearly HFC-134a emissions for synthetic inversions performed using the observations with added (b) high and (c) low magnitude noise. The added noise leads to high and low model-data mismatch errors plotted for the CMN station.

modelled mixing ratios by the transport model [7]. To avoid such bias, we adopted a similar approach to Vojta et al [10], filtering the real observation dataset to include only observations with a model-data mismatch within the ±5 ppt range in the inversion. This likely removed relatively high observation values affected by local sources, up-slope winds or boundary layer dynamics.

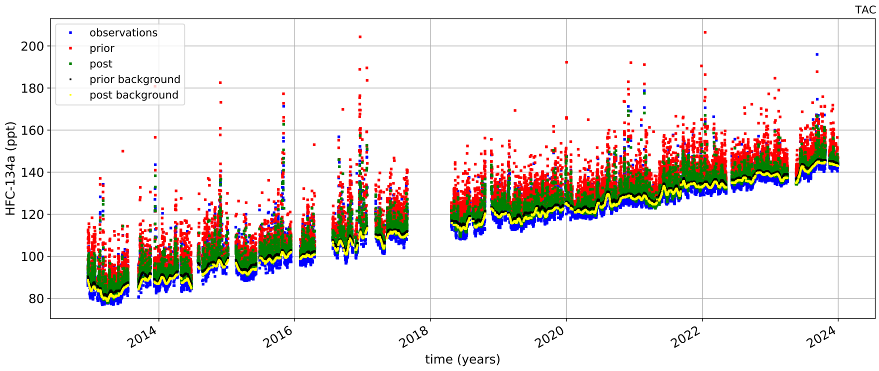

Fig. 5: The modelled prior and posterior mixing ratios compared against the observations for the measurement site of Tacolnestone (TAC).

5 Inversion model performance

Fig. 6 presents a Taylor diagram illustrating improvements in Pearson correlation and root mean squared (RMS) error for modelled mixing ratios across all ground measurement sites over all years. Across all years, the Pearson correlation for the prior modelled mixing ratios ranged from 0.74 to 0.89 for CMN, 0.68 to 0.83 for JFJ, 0.9 to 0.95 for MHD, and 0.74 to 0.9 for TAC. Following inversion, the Pearson correlation for posterior modelled mixing ratios improved to 0.81-0.93 for CMN, 0.71-0.88 for JFJ, and 0.86-0.96 for TAC. MHD did not show any substantial improvements. However, it had the highest Pearson correlation values in the range of 0.91 to 0.95. Fig. 5 shows the modelled prior and posterior mixing ratios compared with the observations for the TAC station.

Fig. 7a shows the difference between *a posteriori* and *a priori* emission fluxes for 2022. It highlights the areas that are estimated to be over or under-emitting with respect to the prior fluxes. Fig. 7b highlights the Italian domain and its disparities with the prior emission fluxes. Lastly, in Fig. 7c, we observe a notable reduction in relative errors after inversion within areas well-covered by emission footprints for 2022.

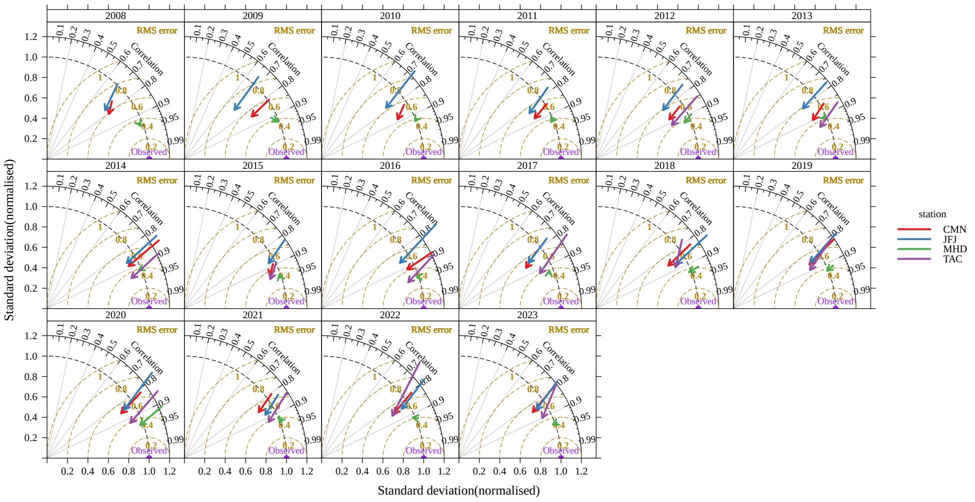

Fig. 6: Taylor diagrams for comparing the prior and posterior simulated mixing ratios with observed mixing ratios for all the measurement stations and the years 2008-2023. Each arrow represents a station where the tail is prior and the head represents the posterior simulated mixing ratio. The radius along the x-axis and y-axis represents the normalised standard deviation against the mean mixing ratio. The azimuthal angle represents the Pearson correlation coefficient. The normalised (against observations) root mean square error (RMS) in the simulated mixing ratios is proportional to the distance from the point labelled "observed" (purple dot) on the x-axis which serves as a reference.

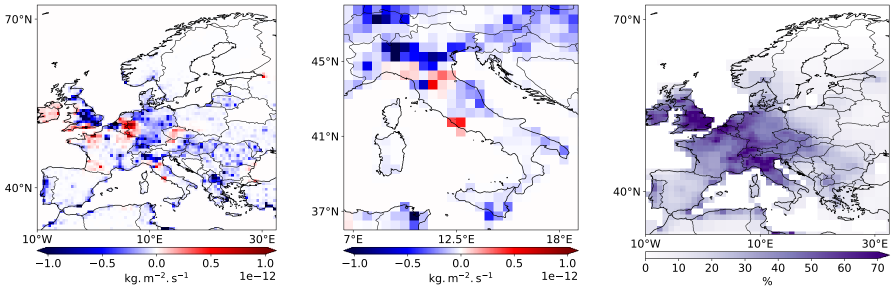

(a)

(b)

(c)

Fig. 7: Disparities between the posterior and prior fluxes in the study domain (a), a close-up view of Italy (b), and the relative reductions in error in the posterior estimates (c) for 2022.

Table 2: The statistical parameters used to check the reliability of the inversions calculated against the observations. The table shows the number of observations (n) used in the inversion for each year, reduced χ^2 value, Pearson correlation (r), and root mean squared error (RMSE) of the posterior modelled mixing ratio for each station calculated against the observations.

Year	n	χ^2	r				RMSE [ppt]			
			(CMN)	(JFJ)	(MHD)	(TAC)	(CMN)	(JFJ)	(MHD)	(TAC)
2008	3736	0.95	0.81	0.76	0.94	-	2.44	2.20	1.31	-
2009	3409	0.97	0.85	0.71	0.93	-	2.38	2.34	1.33	-
2010	3960	0.98	0.89	0.78	0.93	-	2.39	2.15	1.41	-
2011	4759	0.86	0.88	0.84	0.93	-	2.47	2.02	1.17	-
2012	4957	0.91	0.88	0.81	0.92	0.91	2.34	2.01	1.28	3.09
2013	4904	1.25	0.9	0.81	0.92	0.94	2.32	2.11	1.65	2.70
2014	5029	1.23	0.89	0.87	0.92	0.94	2.31	2.2	1.51	2.78
2015	5594	1.11	0.93	0.88	0.94	0.95	2.29	1.88	1.47	2.77
2016	5296	1.08	0.91	0.86	0.95	0.96	2.23	1.97	1.46	2.90
2017	5274	1.07	0.85	0.83	0.92	0.86	2.40	1.98	1.35	2.67
2018	5803	1.13	0.86	0.87	0.93	0.89	2.24	2.06	1.58	2.71
2019	6339	1.10	0.86	0.86	0.93	0.89	2.13	1.91	1.65	2.56
2020	6483	1.06	0.85	0.85	0.94	0.92	2.13	1.98	1.52	2.38
2021	6133	1.01	0.85	0.88	0.94	0.92	2.1	1.77	1.42	2.47
2022	6265	1.09	0.85	0.85	0.91	0.86	2.23	1.8	1.48	2.48
2023	5363	1.05	0.85	0.85	0.94	0.9	2.06	1.92	1.43	2.35

6 Italian national emission inventories

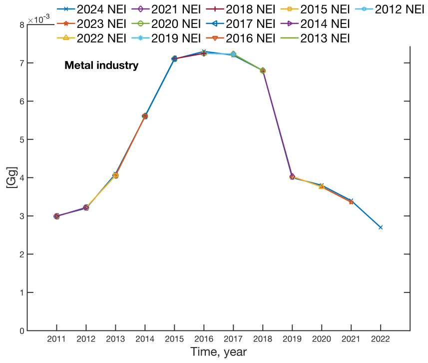

Fig. 8: Comparisons among HFC-134a emissions related to magnesium production for the Italian national emission inventories (NEIs) from 2008 to 2022. No emissions in the time range 2008–2010. Own elaboration based on data from https://unfccc.int/ghg-inventories-annex-i-parties/2024.

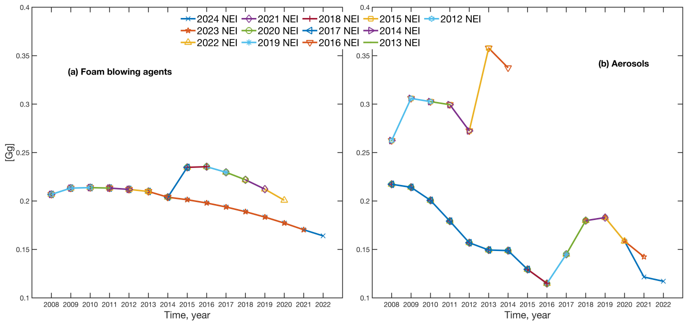

Fig. 9: Comparisons among HFC-134a emissions related to (a) foam blowing agents, and (b) aerosols for the Italian national emission inventories (NEIs) from 2008 to 2022. Own elaboration based on data from https://unfccc.int/ghg-inventories-annex-i-parties/2024.

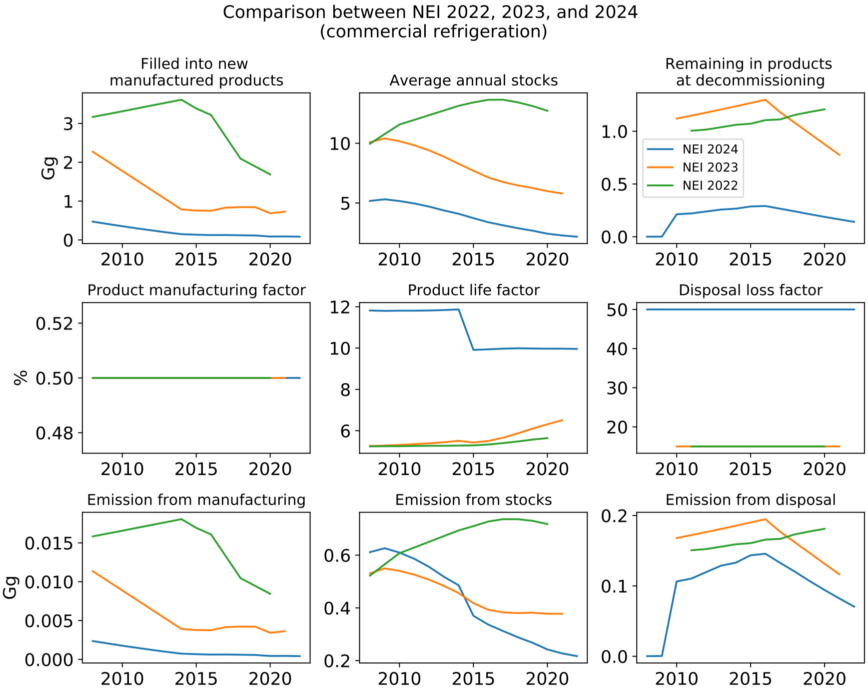

Fig. 10: Comparisons among 2022, 2023, and 2024 Italian national emission inventories (NEIs) activity data (row 1), implied emission factors (row 2), and annual emissions (row 3) for the manufacturing (column 1), stocks (column 2), and disposal (column 3) of commercial refrigeration. Own elaboration based on data from https://unfccc.int/ghg-inventories-annex-i-parties/2024.

7 Seasonal trend

For the whole dataset, the long-term trends were assessed based on singular spectrum analysis [3]. This method assumes an additive decomposition of the data given by long-term and seasonal trends and the residuals. The long-term trends were discarded, and the one-way unbalanced ANOVA-analysis of variance test was computed for the sum of the seasonal trends and the residuals for the dataset by months. The test showed statistically significant differences, p-values below 0.001, among observed mixing ratios -higher in summer months.

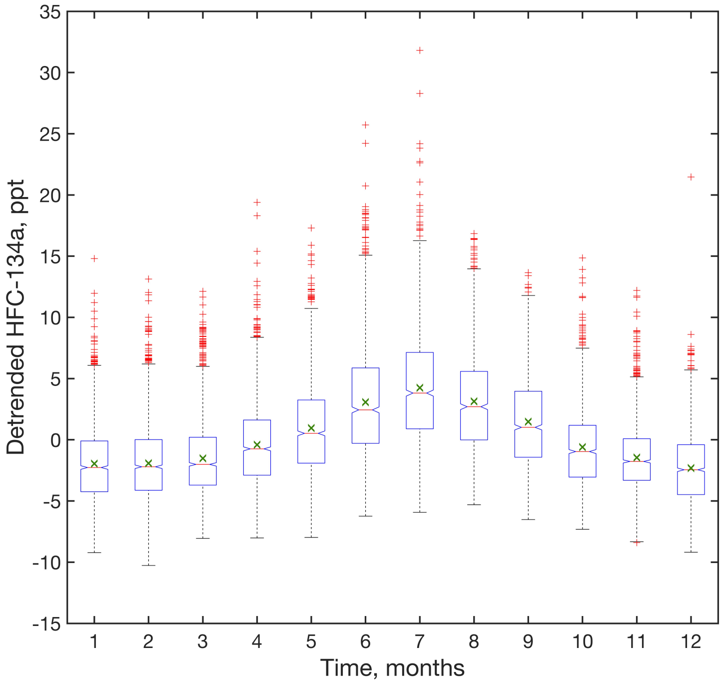

Fig. 11: Comparison of monthly detrended means of HFC-134a: box and whiskers plot with outliers

References

[1] Cesari R, Paradisi P, Allegrini P (2014) Source identification by a statistical analysis of backward trajectories based on peak pollution events. International Journal of Environment and Pollution 55(1-4):94 – 103. https://doi.org/10.1504/ijep.2014.065909

[2] EEA (2023) Fluorinated greenhouse gases 2023. data reported by companies on the production, import, export and destruction of fluorinated greenhouse gases in the european union, 2007-2022. eea report no 04/2023. luxembourg: Publications office of the european union

[3] Golyandina N, Zhigljavsky A (2013) Singular Spectrum Analysis for Time Series. SpringerBriefs in Statistics, Springer, Berlin, Heidelberg, https://doi.org/10.1007/978-3-642-34913-3

[4] Maione M, Giostra U, Arduini J, et al (2013) Ten years of continuous observations of stratospheric ozone depleting gases at monte cimone (italy)—comments on the effectiveness of the montreal protocol from a regional perspective. Science of the total environment 445:155–164

[5] Miller BR, Weiss RF, Salameh PK, et al (2008) Medusa: A sample preconcentration and gc/ms detector system for in situ measurements of atmospheric trace halocarbons, hydrocarbons, and sulfur compounds. Analytical Chemistry 80(5):1536–1545

[6] Seibert P, Frank A (2004) Source-receptor matrix calculation with a Lagrangian particle dispersion model in backward mode. Atmospheric Chemistry and Physics 4(1):51–63. https://doi.org/10.5194/acp-4-51-2004, publisher: Copernicus GmbH

[7] Stohl A, Seibert P, Arduini J, et al (2009) An analytical inversion method for determining regional and global emissions of greenhouse gases: Sensitivity studies and application to halocarbons. Atmospheric Chemistry and Physics 9(5):1597–1620

[8] Thacker WC (2007) Data assimilation with inequality constraints. Ocean Modelling 16(3):264–276. https://doi.org/10.1016/j.ocemod.2006.11.001

[9] Thompson RL, Stohl A (2014) FLEXINVERT: an atmospheric Bayesian inversion framework for determining surface fluxes of trace species using an optimized grid. Geoscientific Model Development 7(5):2223–2242. https://doi.org/10.5194/gmd-7-2223-2014, publisher: Copernicus GmbH

[10] Vojta M, Plach A, Annadate S, et al (2024) A global re-analysis of regionally resolved emissions and atmospheric mole fractions of sf 6 for the period 2005–2021 (preprint). EGUsphere 2024:1–48